Mesoscopic pinning forces in neutron star crusts

S. Seveso,[1,2] P. M. Pizzochero,[1,2]★ F. Grill[1,2] and B. Haskell[3]

[1]*Dipartimento di Fisica, Università degli Studi di Milano, Via Celoria 16, I-20133 Milano, Italy*
[2]*Istituto Nazionale di Fisica Nucleare, sezione di Milano, Via Celoria 16, I-20133 Milano, Italy*
[3]*School of Physics, The University of Melbourne, Parkville, VIC 3010, Australia*

ABSTRACT

The crust of a neutron star is thought to be comprised of a lattice of nuclei immersed in a sea of free electrons and neutrons. As the neutrons are superfluid, their angular momentum is carried by an array of quantized vortices. These vortices can pin to the nuclear lattice and prevent the neutron superfluid from spinning down, allowing it to store angular momentum which can then be released catastrophically, giving rise to a pulsar glitch. A crucial ingredient for this model is the maximum pinning force that the lattice can exert on the vortices, as this allows us to estimate the angular momentum that can be exchanged during a glitch. In this paper, we perform, for the first time, a detailed and quantitative calculation of the pinning force *per unit length* acting on a vortex immersed in the crust and resulting from the mesoscopic vortex–lattice interaction. We consider realistic vortex tensions, allow for displacement of the nuclei and average over all possible orientations of the crystal with respect to the vortex. We find that, as expected, the mesoscopic pinning force becomes weaker for longer vortices and is generally much smaller than previous estimates, based on vortices aligned with the crystal. Nevertheless, the forces we obtain still have maximum values of the order of $f_{pin} \approx 10^{15}$ dyn cm^{-1}, which would still allow for enough angular momentum to be stored in the crust to explain large Vela glitches, if part of the star is decoupled during the event.

Key words: dense matter – stars: neutron – pulsars: general.

1 INTRODUCTION

The physics of the neutron star (NS) crust plays a crucial role when attempting to model these objects. First of all, the outer layers of the star provide a heat blanket that shields the hot interior and determines the observable thermal emission from the surface (Gudmundsson, Pethick & Epstein 1983). The elastic properties of the crust are also crucial, as 'crust quakes' have been invoked to explain a number of phenomena, such as magnetar flares (Thompson & Duncan 1995) and pulsar glitches (Alpar et al. 1994; Middleditch et al. 2006). Furthermore, the crust may sustain a large enough strain to build a 'mountain' that leads to detectable gravitational wave emission (Bildsten 1998). In this paper, we focus on the relation between crustal physics and pulsar glitches.

Glitches are sudden increases in frequency (instantaneous to the accuracy of the data) of an otherwise smoothly spinning down radio pulsar. After the event, there is, in many cases, an increase in the spin-down rate that relaxes exponentially back to the pre-glitch spin-down (Espinoza et al. 2011). Soon after the first observations, the long time-scales associated with this relaxation (up to months) were associated with the re-coupling of a loosely coupled superfluid component in the NS crust (Baym et al. 1969). Neutron superfluidity

in NS interiors is, in fact, expected on a theoretical basis (Migdal 1959) as most of the star will be cold enough for neutrons to form Cooper pairs and behave as a superfluid condensate, which can flow with little or no viscosity relative to the 'normal' component of the crust. Furthermore, recent observations of the cooling of the young NS in the supernova remnant Cassiopea A are consistent with this picture (Page et al. 2011; Shternin et al. 2011; Elshamouty et al. 2013).

A crucial aspect of superfluid dynamics is that the neutron condensate can only rotate by forming an array of quantized vortices, which determine an average rotation rate for the fluid. For the superfluid to spin-down, it is necessary for vorticity to be expelled. If vortices are, however, strongly attracted to the ions in the crust (i.e. they are 'pinned'), their motion is impeded and the superfluid cannot follow the spin-down of the crust, and stores angular momentum, releasing it catastrophically during a glitch (Anderson & Itoh 1975).

The nature of the trigger for vortex unpinning is still debated, with proposals ranging from vortex avalanches (Alpar et al. 1996; Warszawski & Melatos 2013) to hydrodynamical instabilities (Glampedakis & Andersson 2009) or crust quakes (Ruderman 1969, 1976; Alpar et al. 1994; Middleditch et al. 2006). Whatever the trigger mechanism (for a recent review see Haskell & Melatos 2015a), an important ingredient in this picture is the maximum pinning force that the crust can exert on a vortex, before

hydrodynamical lift forces (the Magnus force) are able to free it. This quantity obviously determines the maximum amount of angular momentum that can be exchanged during a glitch. An understanding of how much angular momentum can be stored in different regions of the star would, in fact, allow detailed comparisons with observations of glitching pulsars and potentially constrain the equation of state of dense matter (Andersson et al. 2012; Chamel 2013; Newton, Berger, & Haskell, 2015; Piekarewickz, Fattoyev & Horowitz 2014).

Early theoretical work focused on the microscopic interaction between a vortex and a single pinning site (Alpar 1977; Epstein & Baym 1988). The pinning force *per unit length* of a vortex depends, however, on the mesoscopic interaction between the vortex and many pinning sites, and thus on the rigidity of the vortex, on its radius (represented by the superfluid coherence length ξ) and on the lattice spacing. This naturally leads to the possibility of different pinning regimes in different regions of the crust. Alpar et al. (1984a,b) interpreted the slow post-glitch recovery of the Vela pulsar in terms of vortex 'creep', i.e. thermally activated motion of pinned vortices, and distinguished between three regimes: strong, weak and superweak pinning. The different regimes depend on the interplay between the quantities mentioned earlier: in strong pinning the coherence length ξ of a vortex is smaller than the lattice spacing, and the interaction is strong enough to displace nuclei, while in the weak pinning regime this is not the case. Superweak pinning, on the other hand, comes about when the coherence length ξ is greater than the lattice spacing and a vortex can encompass several nuclei. In this case, there is little change in energy as the vortex moves and thus no preferred configuration for pinning. The pinning force is expected to be weak and, in the limit of infinitely long vortices, all configurations are equal and there would be no pinning (Jones 1991). Fits to the post-glitch relaxation of the Vela pulsar, within the vortex creep framework (Alpar et al. 1984a), were used to set observational constraints on some of these parameters, leading to the conclusion that only weak and superweak pinning are likely to be at work in an NS crust (Alpar et al. 1984b). The theoretical calculations of the mesoscopic pinning force relied, however, on estimates in the weak pinning case for the very particular configuration of vortices *aligned* with the crystal axis. Although very little is known about the defect structure of the crust, one does not in general expect the crystal lattice to be oriented in the same direction over the whole length of a vortex (note also that a vortex will have cylindrical symmetry set by the rotation axis, while the only preferred direction for the crystal will be set by gravity and pressure which have spherical symmetry, slightly modified by rotation). More recently, Link (2009) has performed simulations of motion of a vortex in a three-dimensional random potential, and found that the rigidity of the vortex does, indeed, play a fundamental role in setting the maximum superfluid flow above which vortices cannot remain pinned. Link & Cutler (2002) and Link (2012) also estimated the pinning force per unit length of a rigid vortex in a random lattice using a variational approach, also including phenomenologically the effect of strong entrainment in the crust (Link 2014).

In this paper, we perform a realistic calculation of the mesoscopic pinning force, that is the force per unit length acting on straight vortices in the NS crust. We consider for the first time a micro physically motivated model for the crust and investigate the density dependence of the pinning force. We average over all possible vortex–crystal orientations and show that, although the force is considerably weaker than previous estimates based on particular configurations, it could still be strong enough to account for angular momentum transfer in large pulsar glitches.

2 LATTICE PROPERTIES

The crust of an NS is thought to form a crystal in which completely ionized neutron-rich nuclei form a *body centred cubic* (BCC) lattice, immersed in a sea of electrons and free neutrons. In this configuration, each nucleus is at the centre of a cubic cell of side $s = 2R_{ws}$ with nuclei at each vertex. The separation between the ions (i.e. the potential pinning sites) thus depends on R_{ws}, the radius of the Wigner–Seitz cell, which is a function of the density ρ. In our calculation, we use the classic results from Negele & Vautherin (1973) where the crust is divided into five zones, each one characterized by a specific value of R_{ws} and R_N, which is the radius of the nucleus that occupies a single site of the lattice. Table 1 summarizes these results, together with the nuclear composition of the Wigner–Seitz cells.

Note that there is still significant uncertainty on the exact composition and structure of the crust (Piekarewickz et al. 2014; Steiner et al. 2014) and not only electrons, but also free neutrons, may partially screen the Coulomb interaction between the nuclear clusters, leading to different, and more inhomogeneous, configurations than a BCC lattice (Kobyakov & Pethick 2014). Nevertheless, the procedure we describe below can easily be adapted to different configurations.

To calculate the mesoscopic pinning force, we need to identify the configurations in which the vortex is most strongly pinned to the lattice and the configurations in which it is 'free' (note that a vortex is never truly free, as it will always intersect pinning centres. The 'free' configuration simply represents the average energy configuration between locations of maximum pinning, as discussed in the next section). Once this has been done, the *maximum* pinning force F_p simply follows from

$$F_p = \frac{E_{free} - E_{pin}}{\Delta r}, \qquad (1)$$

where E_{pin} is the energy of the most strongly pinned configuration and E_{free} the energy of the free configuration. The average distance the vortex has to move between the configurations is Δr.

The energy of a particular vortex configuration will depend on the number of ions that it is able to pin to. Intuitively, the more sites it can pin to, the greater the energy gain, the stronger the pinning. In order to perform the calculation, it is thus necessary to consider the pinning energy *per pinning site* E_p, i.e. the amount by which the energy of the system is changed when a single nucleus is inside the vortex. This quantity depends on the competition between the kinetic energy and the condensation energy of the superfluid, which is strongly density dependent and will thus change if a dense nucleus is introduced in the vortex. In this work, we use the results of Donati & Pizzochero (2003, 2004, 2006), who calculate E_p consistently in the local density approximation. The values of E_p for different densities are given in the last columns of Table 1. Note that in some regions E_p is positive, i.e. it costs energy to introduce a nucleus in a vortex. In these regions, the vortex–nucleus interaction is repulsive and one has 'interstitial' pinning (IP), in which the favoured vortex configurations are in-between nuclei. We refer to the case in which the interaction between nuclei and vortices is attractive as 'nuclear' pinning (NP). We shall see in the following that the effect of attraction or repulsion does not strongly influence the calculation of the mesoscopic pinning force. The parameter β refers to the suppression factor for the neutron pairing gap used in the calculations: $\Delta = \frac{\Delta_0}{\beta}$, where Δ_0 is the pairing gap of the superfluid obtained by using the bare interaction (i.e. not accounting for in-medium corrections). This factor is related to the

Table 1. Fiducial values of the quantities used in our calculations. These values are taken from Negele & Vautherin (1973): the NS crust is divided into five zones and here we give the baryon density ρ, the Wigner–Seitz cell radius (R_{ws}), the element corresponding to the cell nuclear composition, the nuclear radius (R_N), the superfluid coherence length (ξ), which represents the vortex radius, and the pinning energy per site (E_p). The last two quantities are taken from the results of Donati & Pizzochero (2004, 2006).

No.	ρ (g cm^{-3})	Element	R_{ws} (fm)	R_N (fm)	ξ (fm)		E_p (MeV)	
					$\beta = 1$	$\beta = 3$	$\beta = 1$	$\beta = 3$
1	1.5×10^{12}	$^{320}_{40}$Zr	44.0	6.0	6.7	20.0	2.63	0.21
2	9.6×10^{12}	$^{1100}_{50}$Sn	35.5	6.7	4.4	13.0	1.55	0.29
3	3.4×10^{13}	$^{1800}_{50}$Sn	27.0	7.3	5.2	15.4	−5.21	−2.74
4	7.8×10^{13}	$^{1500}_{40}$Zr	19.4	6.7	11.3	33.5	−5.06	−0.72
5	1.3×10^{14}	$^{982}_{32}$Ge	13.8	5.2	38.8	116.4	−0.35	−0.02

polarization effects of matter on the nuclear interaction. The case $\beta = 1$ describes the non-polarized interaction, while the case $\beta = 3$ describes the one in which the effect of the polarization is maximum. When $\beta = 1$, the mean pairing gap has a maximum of about 3 MeV, which corresponds to the strong pairing scenario, while when $\beta = 3$ the mean pairing gap has a maximum of about 1 MeV, as usually assumed in the weak pairing scenario. Realistic Monte Carlo simulations of neutron matter (Gandolfi et al. 2008) indicate a reduction of the pairing gap consistent with the choice $\beta = 3$.

The total energy of the interaction between a given vortex portion and the lattice is calculated summing the contribution of each nucleus that can be captured by the pinning force. Naively, this could be done by considering the vortex as a cylinder of radius ξ and counting how many nuclei are contained within it (we will discuss how to count nuclei at the boundary in the following). This approach can be improved to take into account the possible deformation of the nuclear lattice. The lattice has elastic properties, so it is possible for nuclei to be displaced from their equilibrium position under the action of the pinning force. The resulting energy per site can be expressed as

$$E(r) = E_p + E_1(r), \tag{2}$$

where r is the distance of the vortex axis from the equilibrium position of the considered nucleus. In this approach, the pinning energy per site E_p is corrected by the factor $E_1(r)$ that encodes the change in electrostatic energy due to the displacement of the nucleus. We will then define the capture radius r_c as the radius within which it is energetically favourable for the nuclei to be displaced: this will be the radius of the vortex to be used in the counting procedure. Let us now estimate r_c for both NP and IP.

2.1 Nuclear pinning

In the NP regime ($E_p < 0$), we define a pinning region assuming that a nucleus contributes to the total interaction by a factor E_p if it is completely inside the vortex: in other words, its distance from the vortex axis must be less than $\gamma = \xi - R_N$ (Fig. 1), with $\gamma = 0$ if $\xi < R_N$. If a site is at a distance $r > \gamma$ from the vortex axis, the nucleus must be dragged by a distance $\delta(r) = r - \gamma$. The electrostatic energy is calculated in a standard way using Gauss theorem together with the Wigner–Seitz approximation, which divides the lattice into independent spherical cells of radius R_{ws}, each with an ion in the centre surrounded by the electron and neutron gas:

$$E_1(r) = \frac{Z^2 e^2}{2 R_{ws}^3} \delta^2(r), \tag{3}$$

where e is the elementary charge and Z is the number of protons and electrons in the cell. Of course, a nucleus whose equilibrium position
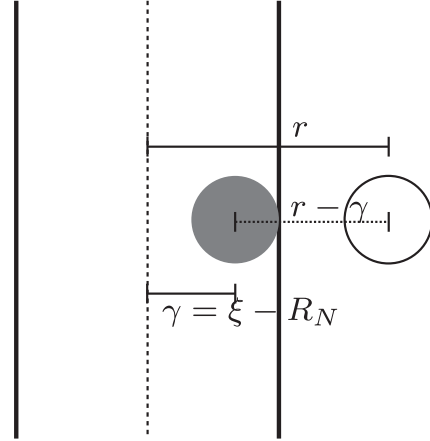

Figure 1. Representation of a nucleus displacement (NP case). The open and full circles represent, respectively, the starting and final position of the nucleus. The dashed line represents the displacement $\delta(r)$.

is already inside the pinning region does not need to be dragged, so its energy contribution has no electrostatic term ($E(r) = E_p$ if $r < \gamma$). We can now define the maximum drag distance r_0 as the value of $\delta(r)$ for which the effective pinning interaction of equation (2) becomes zero:

$$r_0 = \sqrt{-\frac{2 E_p R_{ws}^3}{Z^2 e^2}}. \tag{4}$$

From these consideration, it follows that the final *capture radius* that must be used in our calculation will be

$$r_c = \gamma + r_0 = \xi - R_N + r_0. \tag{5}$$

The total energy of the interaction between the considered vortex portion (of length L) and the lattice is calculated summing the contribution of each nucleus that can be captured by the pinning force. This energy is calculated through an integral over a uniform distribution of nuclei, which is valid when the number of nuclei which are taken into account becomes very large, so for $L \gg R_{ws}$. Given N the number of pinning sites that fall inside a cylinder of radius r_c and length L, the superficial density will be $n_N = \frac{N}{\pi r_c^2}$. Then the total energy is calculated as

$$E = \int_0^\gamma E_p n_N \, 2\pi r \, dr + \int_\gamma^{\gamma + r_0} (E_p + E_1(r)) \, n_N \, 2\pi r \, dr$$

$$= \frac{N E_p}{(\gamma + r_0)^2} \left(\gamma^2 + \frac{4}{3} \gamma r_0 + \frac{1}{2} r_0^2 \right). \tag{6}$$

Table 2. Lattice properties for the five zones of Table 1. The values in Table 1 are used here to calculate the capture radius r_c (in units of R_{ws}) and the effective pinning energy per site E_{eff} as explained in Section 2.

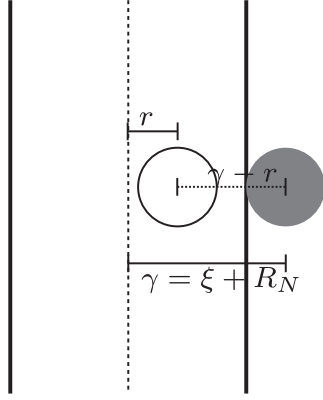|				$\beta = 1$					$\beta = 3$		
No.	IP/NP	γ (fm)	r_0 (fm)	r_c (R_{ws})	E_p (MeV)	E_{eff} (MeV)	γ (fm)	r_0 (fm)	r_c (R_{ws})	E_p (MeV)	E_{eff} (MeV)
1	IP	12.7	14.0	0.289	2.63	0.36	26.0	3.9	0.591	0.21	0.17
2	IP	11.1	6.2	0.313	1.55	0.64	19.7	2.7	0.555	0.29	0.24
3	NP	0.0	7.6	0.204	−5.21	−2.60	8.1	5.5	0.504	−2.74	−2.08
4	NP	4.6	5.7	0.531	−5.06	−3.46	26.8	2.1	1.490	−0.72	−0.69
5	NP	33.6	1.1	2.514	−0.35	−0.34	111.2	0.3	8.080	−0.02	−0.02

Figure 2. Representation of a nucleus displacement (IP case). The open and full circles represent, respectively, the starting and final position of the nucleus. The dashed line represents the displacement $\delta(r)$.

From this equation, we can immediately evaluate the effective interaction energy *per site* E_{eff}, defined by $E = NE_{eff}$:

$$E_{eff} = \frac{E_p}{(\gamma + r_0)^2} \left(\gamma^2 + \frac{4}{3}\gamma r_0 + \frac{1}{2}r_0^2 \right). \tag{7}$$

In Table 2, we give the values of the above quantities, which have been calculated using the fiducial inner crust and superfluid properties of Table 1.

2.2 Interstitial pinning

The evaluation of r_c and E_{eff} in the IP regime ($E_p > 0$) follows the same steps of the previous section, but taking into account the fact that in this case the interaction is repulsive and thence a nucleus that lies in the vortex core must be expelled instead of dragged into it in order to lower the energy. We define a nucleus as expelled if it is completely outside the vortex, that is if its distance from the vortex axis is larger than $\gamma = \xi + R_N$ (Fig. 2); a nucleus which is expelled does not contribute to the pinning energy. The drag distance now is $\delta(r) = \gamma - r$ and the maximum value for this quantity, r_0, is given by the energy balance $E_p = E_l(\delta = r_0)$. This encodes the idea that the nuclear displacement is favourable until the energy of the dragged nucleus configuration is lower than the energy of the configuration where the nucleus is still in its equilibrium position in the lattice:

$$r_0 = \sqrt{\frac{2E_p R_{ws}^3}{Z^2 e^2}}. \tag{8}$$

The capture radius that must be used in the counting procedure in this case is equal to γ because the nuclei that contribute to the pinning energy are only those that lie in the pinning region
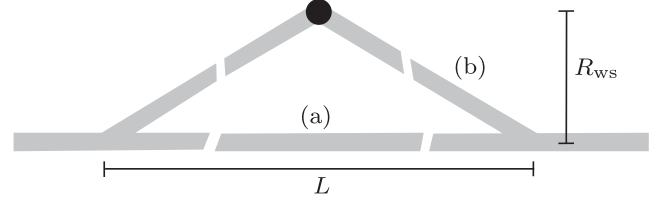
$$r_c = \gamma = \xi + R_N. \tag{9}$$

Figure 3. Representation of the vortex deformation. We sketch a rigid vortex (a) and a bent vortex (b). L is the vortex length and R_{ws} is the Wigner–Seitz radius. Note that a realistic vortex configuration will not have any kinks, and these appear here simply for ease of plotting.

Now, if $r_0 < \gamma$, the total energy is calculated as

$$E = \int_0^{\gamma - r_0} E_p n_N 2\pi r \, dr + \int_{\gamma - r_0}^{\gamma} E_l(r) n_N 2\pi r \, dr, \tag{10}$$

where the second term of the integral contains only the electrostatic contribution because the nuclei in that region have been expelled. If instead $r_0 > \gamma$, all the nuclei that contribute to the pinning energy are dragged outside the vortex: in this case, we have

$$E = \int_0^{\gamma} E_l(r) n_N 2\pi r \, dr. \tag{11}$$

Solving these integrals and defining again $E = NE_{eff}$, we obtain the effective pinning energy *per site* (see Table 2 for numerical results):

$$E_{eff} = \begin{cases} E_p \frac{1}{\gamma^2} \left(\gamma^2 - \frac{4}{3}\gamma r_0 + \frac{1}{2}r_0^2 \right) & r_0 \leq \gamma \\ E_p \frac{\gamma^2}{6r_0^2} & r_0 > \gamma. \end{cases} \tag{12}$$

2.3 Vortex length

The length-scale over which a vortex can be considered straight corresponds the length L of the cylinder on which we perform the counting procedure described. We can estimate the order of magnitude of L with a simple argument based on energy considerations (we develop the argument in the NP regime, but the same result obtains in the IP regime). Assuming that the vortex, under tension T (self-energy per unit length), will bend under the influence of the pinning force, we can equate the energy of two limiting configurations: the straight (infinitely rigid) vortex (Fig. 3a) and the vortex that has bent in order to pin to an additional nucleus at a typical distance of the order of R_{ws} (Fig. 3b):

$$TL = E_p + T(L + \Delta L). \tag{13}$$

The difference ΔL of the vortex length in the two configurations is obviously

$$\Delta L = 2\sqrt{\left(\frac{L}{2}\right)^2 + R_{ws}^2} - L \approx \frac{2R_{ws}^2}{L}, \tag{14}$$

where we have expanded the expression following the realistic assumption that $R_{ws} \ll L$. Finally, we have

$$\frac{L}{R_{ws}} = \frac{2 T R_{ws}}{|E_p|} \sim 10^3, \tag{15}$$

where the standard NS values have been used: $T \sim 20$ MeV fm^{-1} (Jones [1990]), $R_{ws} \sim 30$ fm and $|E_p| \sim 1$ MeV. We will thus study the dependence of our results on variations of the parameter L around the estimate in equation (15). Note that the ability of a vortex to bend and adapt to a pinned configuration plays an important role in determining the maximum of the pinning force, as also found by Link ([2009]). In particular, we shall see in Section 4.2 that our estimate of $T \sim 20$ MeV fm^{-1} is appropriate for high-density regions at the base of the crust, but that the tension can be much lower at lower densities, leading to vortices being much less rigid and higher values of the pinning force.

Let us point out that this is the length-scale over which a vortex would need to unpin to move to a different configuration, and agrees with the estimate of Link ([2014]) and with the numerical simulations of Hirasawa & Shibazaki ([2001]). In Appendix A, we also present a hydrodynamical calculation of the length-scale over which a rigid vortex can unpin, which agrees with the estimate for L in equation (15). It should not be confused with the average length-scale between pinning bonds, l_p, defined by Link & Cutler ([2002]) and Link ([2012]) which has a different scaling with the parameters. We shall see in the following that our functional form for the pinning force per unit length scales with the tension in the same way as that of Link ([2012]) and will interpret l_p accordingly.

We point out, however, that l_p cannot represent the *actual* distance between successive NP sites as assumed in Link & Cutler ([2002]) and Link ([2012]). Indeed, these author define the rigidity length l_p by the additional constraint that $\pi u^2 l_p n_N = 1$, with $n_N \approx 1/R_{ws}^3$, to determine the vortex lateral deviation u: namely the vortex length must be such that bending defines a volume that contains only one nucleus. In order for this to be consistent, the deviation u must be larger than the vortex core ξ for point-like nuclei, as also explicitly noted in Link & Cutler ([2002], for real nuclei, one should require $u > \xi + R_N$). With standard parameters for the inner crust, however, this consistency condition is never satisfied, making the approach of Link & Cutler ([2002]) and Link ([2012]) physically incorrect. We will come back to this at the end of Section 5.

We finally notice that the choice $u = R_{ws}$ made in the derivation of equation (15) is physically reasonable for a general, order-of-magnitude definition of vortex rigidity since R_{ws} is the natural length-scale of the system, also when pinning is concerned. For example, the pinning energies per site E_p calculated so far and used to estimate the mesoscopic pinning forces correspond to the difference in energy between two configurations (nuclear and interstitial), where the vortex has moved by a distance R_{ws} (Donati & Pizzochero [2003], [2004], [2006]). Moreover, since $2 R_{ws}$ is the average distance between nuclei, displacing a segment of vortex by a distance of the order of R_{ws} will likely intersect a new nucleus. Of course, alternative and more specific choices of the typical deviation u could also be proposed as plausible: for instance, $u = \xi + R_N$ or $u = r_c$. From Tables [1] and [2], we see that these choices would give deviations that, depending on the density and for the more realistic case $\beta = 3$ of weak pinning, can be either larger or smaller than R_{ws} by a factor of less than 2.[1] Because of this ambiguity in the definition of u,
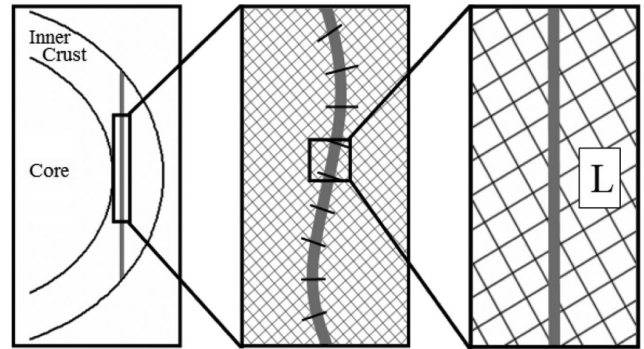

Figure 4. Representation of the vortex rigidity on different scales. L is the maximum length of the unbent vortex as discussed in Section 2.3.

in the following we will show results associated with a range of values of L. However, rescaling the deviation as $u = \alpha R_{ws}$ implies rescaling the rigidity length L by a factor α^2 while, due to the weak dependence $f_L \sim 1/\sqrt{L}$ shown in equation (27), the mesoscopic pinning force f_L is rescaled by a factor α^{-1}. Therefore, although the uncertainty in the choice of u implies uncertainties in the final pinning forces, we expect this error to be less than a factor of 2 so that the orders of magnitude and relative strengths estimated for f_L will still be quite reliable.

3 MESOSCOPIC PINNING FORCE

The calculation of the pinning force per unit length is done here by *counting* the actual number of pinning sites intercepted by a randomly oriented vortex.

We consider vortices parallel to the rotation axis and that thread the whole star. Due to the finite rigidity of the vortex, we assume that it can be considered straight only on a characteristic length-scale L, as described in the previous section (Fig. [4]). This idea, combined with the fact that the lattice is made up by macro-crystals with random direction (Jones [1990]), indicates that a macroscopic portion of vortex immersed in the crust experiences all possible orientations with respect to the lattice. The force per unit length should then be calculated as an average over all angular directions. In following this procedure, we neglect the effects of turbulence, which may arise in NS interiors (Peralta et al. [2005], [2006]; Andersson, Sidery & Comer [2007]), possibly due to modes of oscillations of the superfluid that may be unstable in the presence of pinning (Glampedakis & Andersson [2009]; Link [2012]). In this case, the vortex array is likely to form a complex tangle, which must, however, still be polarized due to the rotation of the star. Given that the problem of polarized turbulence is poorly understood (see Andersson et al. [2007] for the description of a possible approach to this issue), we shall focus on a regular vortex array in this paper, and leave the complex problem of turbulence for future work.

We consider an infinite BCC lattice with its symmetry axes oriented as $\hat{x}$, $\hat{y}$ and $\hat{z}$, and with a nucleus in $(0, 0, 0)$. A vortex is modelled as a cylinder of length L and radius r_c with its median point initially in the origin and the orientation is given by the angles

---

[1] The deepest region, zone 5, has both ξ, $r_c \gg R_{ws}$ so that the choices $u = \xi + R_N$ or $u = r_c$ would give very large L and thence very small

pinning forces, corresponding to the superweak pinning regime of Alpar et al. ([1984a]). Also the choice $u = R_{ws}$, however, leads to very weak pinning at high densities once we consider the density dependence of the tension, as discussed in Section 4.2 and shown in Fig. [13].
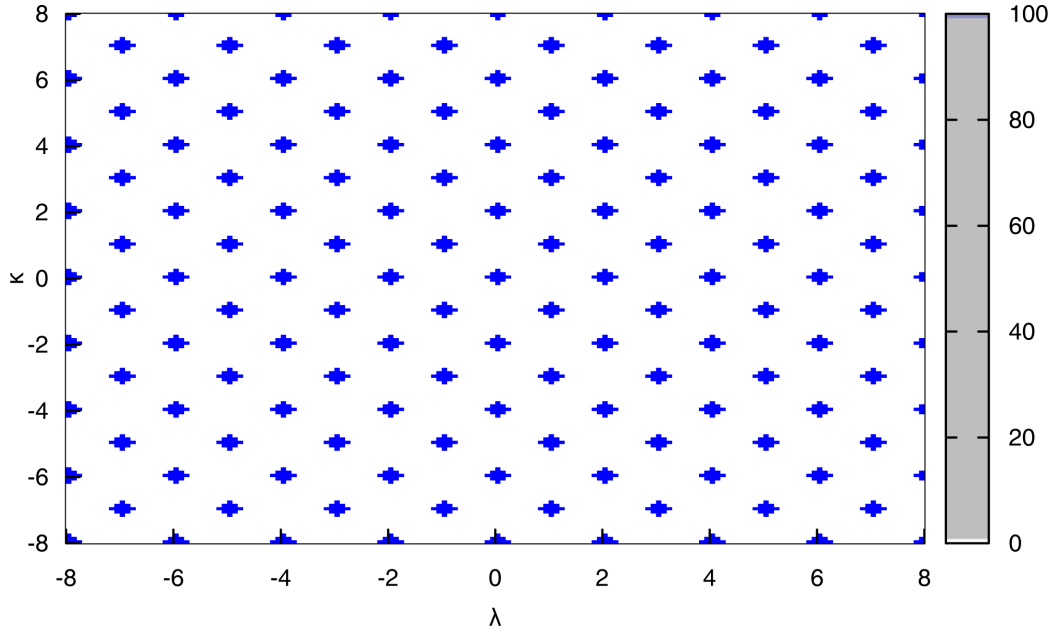
Figure 5. Number of captured pinning sites $N(\lambda, \kappa)$ when the vortex is *aligned* with the lattice. The colour codes are described in the sidebar. The axes λ and κ represent the translation of the vortex with respect to the initial position, and they are measured in R_{ws} units. The grid step size is d$h = 0.1\,R_{ws}$, the vortex is $L = 200\,R_{ws}$ and the capture radius is $r_c = 0.204\,R_{ws}$ (region 3 with $\beta = 1$). Note that the simple geometry leads to several disjoint maxima that spread over several steps, given that for a small grid step dh the energy of the configuration does not change until the vortex has been moved by one capture radius away from the aligned nuclei.
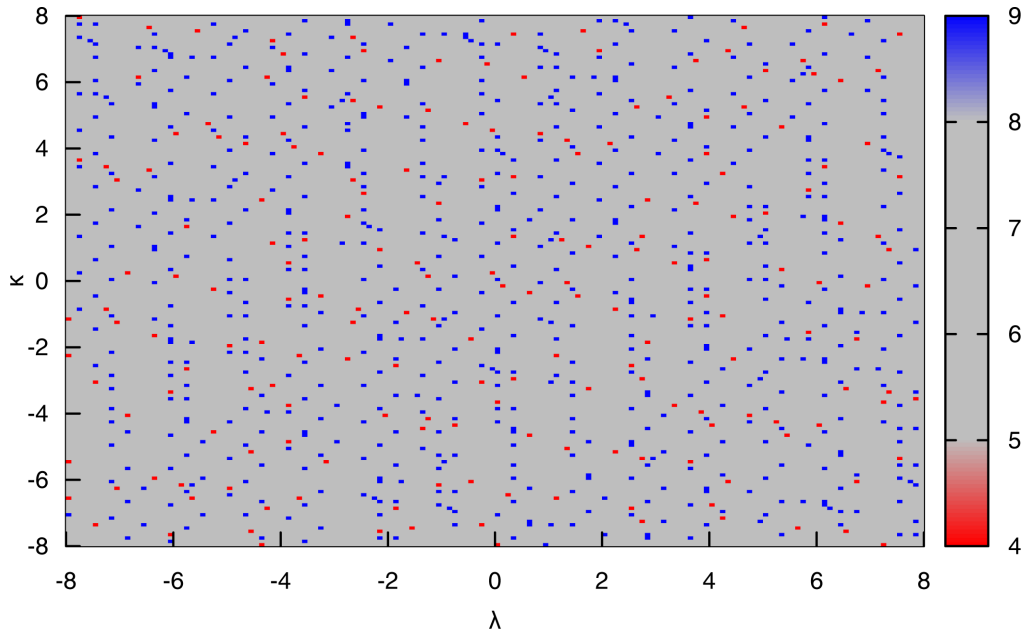

Figure 6. Number of captured pinning sites $N(\lambda, \kappa)$ when the vortex is *non-aligned* with the lattice (we selected a random orientation). The colour codes are described in the sidebar. For details on the parameters used to produce this plot, see Fig. 5.

θ and ϕ in spherical coordinates. For a given choice of θ and ϕ, we evaluate the pinning force per unit length $f_L(\theta, \phi)$ by a counting procedure: from the initial position, the vortex is moved parallel to itself, covering a square region of side l in the plane perpendicular to the vortex axis, with steps of an amount dh. For each new position, identified by the displacement (λ, κ), it is possible to count the number $N(\lambda, \kappa)$ of lattice nuclei that are within the capture radius of the vortex. In Figs 5 and 6, we show two examples of a density plot where for each translation of the vortex (λ, κ) we plot the number of

captured pinning sites $N(\lambda, \kappa)$. The difference between the cases of vortex aligned with the lattice and vortex with arbitrary orientation is evident from the figures.

As discussed in the previous section, the number of captured pinning sites N in a vortex–lattice configuration is directly related to the energy of the configuration by the expression $E = E_{\mathrm{eff}}N$, where E_{eff} is the effective contribution of every single interaction. As previously discussed, the interaction between the vortex and the nuclei can be attractive (NP) or repulsive (IP) in different regions
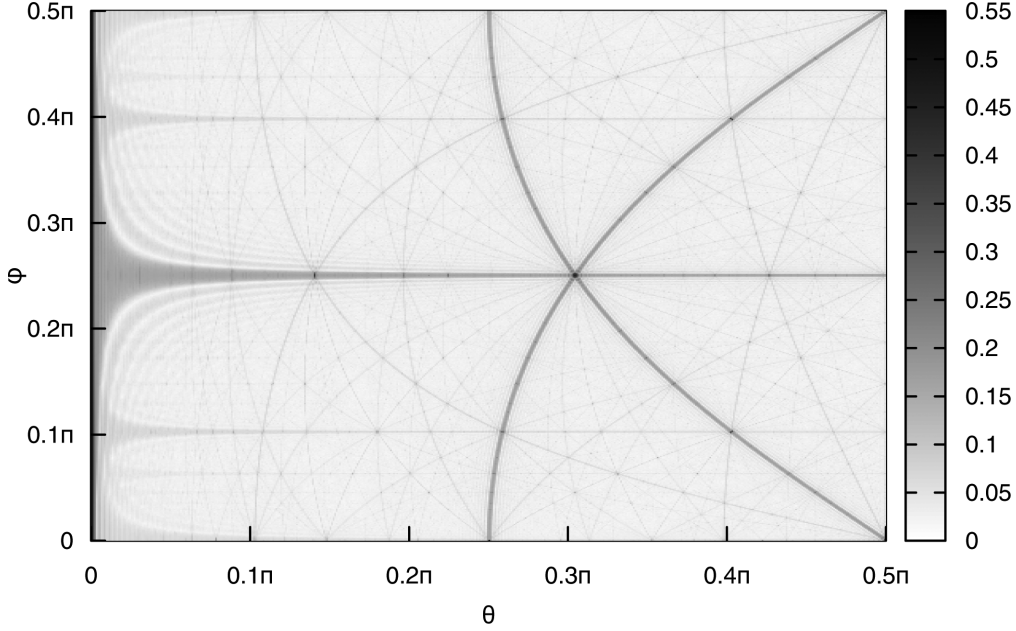
Figure 7. Difference between the number of pinning sites of the free and bound configurations as a function of the vortex orientation (θ, ϕ). Here we plot $|\Delta N(\theta, \phi)|/\tilde{L}$, where $\tilde{L}$ is the (adimensional) vortex length in units of the Wigner–Seitz radius. The colour codes are described in the sidebar. The figure has been obtained considering a vortex of length $L = 200\,R_{\text{ws}}$ and capture radius $r_{\text{c}} = 0.204\,R_{\text{ws}}$ (region 3 with $\beta = 1$).

of the crust. The calculation procedure presented here is valid for both cases, with the following distinction: in the NP regime, the *bound* configuration (state of minimum energy) is identified by the positions (λ, κ) where the number of pinning sites reaches its maximum. This means that $N_{\text{bound}}(\theta, \phi) = \max (N(\lambda, \kappa))$. On the other hand, in the IP case, we must take the minimum: $N_{\text{bound}}(\theta, \phi) = \min (N(\lambda, \kappa))$.

This leads to the fact that, for both the NP and IP cases, the change in energy obtained by moving the vortex away from its bound configuration (unpinning energy) will be

$$\Delta E(\theta, \phi) = E_{\text{eff}} \Delta N(\theta, \phi)$$
$$= E_{\text{eff}} \left(N_{\text{free}}(\theta, \phi) - N_{\text{bound}}(\theta, \phi) \right), \quad (16)$$

where we take N_{free} as the average number of pinning sites counted in all visited displacements: $N_{\text{free}}(\theta, \phi) = \langle N(\lambda, \kappa) \rangle$. Obviously, we have $\Delta E(\theta, \phi) > 0$ for both the NP and IP cases, since it takes energy to remove the vortex from the location where it is pinned. We see that in any given zone (fixed E_{eff} and r_{c}) the unpinning energy depends on the vortex orientation only through $\Delta N(\theta, \phi) = N_{\text{free}}(\theta, \phi) - N_{\text{bound}}(\theta, \phi)$, the change in the number of captured nuclei between the two configurations. In Fig. 7, we plot the quantity $|\Delta N(\theta, \phi)|/\tilde{L}$ as a function of (θ, ϕ), where $\tilde{L} = L/R_{\text{ws}}$ is the (adimensional) vortex length in units of R_{ws}; the plot corresponds to region 3 (NP regime), so that actually $\Delta N(\theta, \phi) < 0$. Notice that the aligned configuration of Fig. 5 would correspond to $\Delta N(0, 0)/\tilde{L} = -0.5$, since $N_{\text{free}}(0, 0) = 0$ and $N_{\text{bound}}(0, 0) = L/2\,R_{\text{ws}}$ (the captured nuclei are a distance $s = 2\,R_{\text{ws}}$ apart). It is evident from the figure that most orientations have $|\Delta N(\theta, \phi)|/\tilde{L} \ll 0.5$.

The force required to move the vortex away from the bound configuration can be easily calculated using the following expression:

$$F(\theta, \phi) = \frac{\Delta E(\theta, \phi)}{D(\theta, \phi)}, \quad (17)$$

where $D(\theta, \phi)$ identifies the average distance required to reach the free configuration from the pinned one. We estimate this quantity

by counting in the density plot the number n_{bound} of disjoint positions where $N(\lambda, \kappa) = N_{\text{bound}}$ (we sometimes omit the angular dependence for notational simplicity). In other words, n_{bound} represents the number of distinct extremal configurations (maxima in the NP regime, minima in the IP regime) found in the sampling square region. For a uniform distribution of these extremal points (square array of step $2D$), we would have $n_{\text{bound}} \pi D^2 \simeq l^2$, where l is the side of the square region tested by parallel-transporting the vortex. We thus take as a reasonable definition for the average distance in the general case:

$$D(\theta, \phi) = \frac{l}{\sqrt{\pi n_{\text{bound}}(\theta, \phi)}}. \quad (18)$$

Finally, the force per unit length is

$$f_L(\theta, \phi) = \frac{F(\theta, \phi)}{L}. \quad (19)$$

For the procedure described above, it is clearly necessary to unambiguously count $n_{\text{bound}}(\theta, \phi)$. With the parallel-transport operation, we explore a portion of the plane that is perpendicular to the vortex axis. This region is a square region of side l that is sampled with a grid of step dh. This means that we have to look for the position of maxima/minima analysing a set of points $(\lambda, \kappa)_{ij} = (-l/2 + i\,dh, -l/2 + j\,dh)$. If we merely count the number of points for which $N_{ij} = N(\lambda, \kappa)_{ij}$ reaches its maximum/minimum value, this result would be strongly conditioned by the choice of the dh parameter. In fact, for small values of dh, it is obvious that a single 'maximum/minimum position' will be split over several points $(\lambda, \kappa)_{ij}$, altering the final result.

One possible solution is to take into account only *disjoint* maxima/minima: this means that two extremal points count as one if they are 'first neighbours'. This approach requires a second-pass analysis over the values N_{ij} to identify the clusters in the density map, and it allows us to correctly evaluate a configuration such as the one in Fig. 5, in which the alignment of the vortex with the symmetry axis of the crystal leads, for small grid steps, to several

neighbouring equivalent configurations. Without considering clustering, we would have counted $n_{\text{bound}} = 1745$ for this particular case ($dh = 0.1 R_{\text{ws}}$). Counting only *disjoint* extremal points, instead, gives the correct answer of $n_{\text{bound}} = 145$, and this result does not change if we explore the square region with a smaller step size.

In this work, the method just described has been slightly generalized to treat extremal points that are topologically disjoint but 'very close' and thence physically equivalent. As described previously, the actual vortex radius (ξ) and the site radius (R_{N}) are encoded together in the single parameter r_{c} because this is the only relevant quantity (from the geometrical point of view) in the evaluation of the number of vortex–lattice interactions for a given configuration. However, the site radius in this picture has still a physical meaning: in order for a nucleus to *actually* enter or exit the vortex core and thus change the vortex–lattice energy, the vortex axis must move by at least $2R_{\text{N}}$. Therefore, if two extremal points are less than $2R_{\text{N}}$ apart, there is no actual change in energy for the vortex to move from one to the other and therefore they must be counted together as a single pinning site. In other words, we choose to count two extremal points as one if their distance is less than a quantity $\eta \sim 2R_{\text{N}}$.

In conclusion, the number $n_{\text{bound}}(\theta, \phi)$ appearing in equation (18) is corrected to take into account the 'clusters' of extremal points as determined by the parameter η: it corresponds to the number of *disjoint* clusters, each representing a physically distinct pinning site. For the five zones in Table 1, the quantity $2R_{\text{N}}$ is always in the range $(0.25–0.75) R_{\text{ws}}$. In order to make the calculations affordable, we fix $\eta = 0.5 R_{\text{ws}}$ for every zone, after testing that there is no significant difference in the final results for the pinning force (below 10 per cent and anyways well within the error bars) under variations of η in the previous range. Altogether, it is evident that the main uncertainty in the calculation of the pinning force comes from the determination of $n_{\text{bound}}(\theta, \phi)$: in order to have some measure of this and since we are dealing with a counting measurement, we will associate with n_{bound} the standard error $\pm\sqrt{n_{\text{bound}}}$.

To obtain the final value f_L for the mesoscopic pinning force, we must repeat the above calculations for each value of (θ, ϕ), and then take the angular average:

$$f_L = \langle f_L(\theta, \phi) \rangle = \frac{1}{4\pi} \int f_L(\theta, \phi) \, d\Omega. \tag{20}$$

An estimate of the error $\pm\sigma_{f_L}$ on f_L can also be obtained, by propagating the error on $n_{\text{bound}}(\theta, \phi)$ in equations (17)–(20).

We also checked that our results are reasonably independent from the choice of the parameters l and dh used in the parallel-transport sampling procedure. In Figs 8 and 9, we show an example of the convergence of the calculated f_L for different values of l and dh. In the following, we will fix $l = 16 R_{\text{ws}}$ and $dh = 0.005 R_{\text{ws}}$, which provide an acceptable accuracy (well within the error bars $\pm\sigma_{f_L}$) while allowing for a not-too-long computational runtime.

4 RESULTS OF THE MODEL: BCC LATTICE

The results of our calculations are summarized in Table 3. We have applied the algorithm described in the previous sections to different choices of the parameter L, starting from a short vortex with length equal to $100 R_{\text{ws}}$ up to a configuration with $L = 5000 R_{\text{ws}}$. For each value of L and for each zone of Table 1, we have calculated the pinning force per unit length f_L and the estimated error σ_{f_L} for two values of the polarization correction factor, $\beta = 1$ (i.e. the case of a bare interaction) and $\beta = 3$, which is close to the value obtained in realistic Monte Carlo simulations of neutron matter (Gandolfi et al. 2008). The results for the pinning force per unit length are also
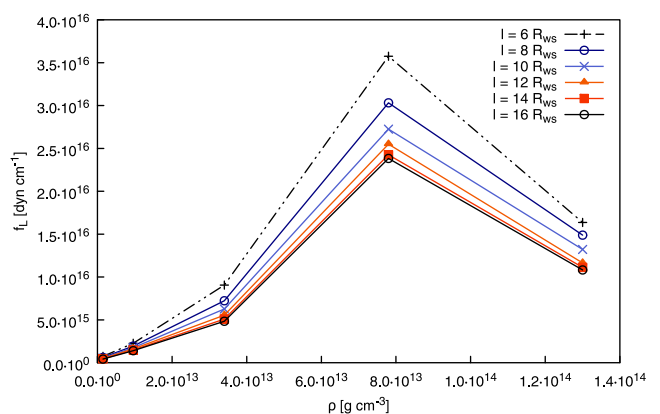
Figure 8. Convergence test for the l parameter used in our calculation. In this figure, we can see the pinning force per unit length for the five zones of the inner crust, obtained with different choices of the parameter: *increasing* the value of l, the curves become closer, showing the convergence of the model. This picture corresponds to a vortex of length $L = 200 R_{\text{ws}}$.
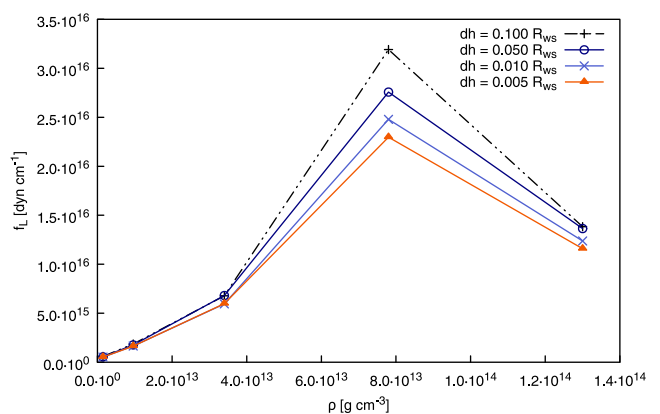
Figure 9. Convergence test for the dh parameter used in our calculation. As in Fig. 8 we can see that *decreasing* the value of dh, the curves become closer, showing the convergence of the model also for this parameter. This picture corresponds to a vortex of length $L = 200 R_{\text{ws}}$.

plotted in Fig. 10 for $\beta = 1$ and in Fig. 11 for $\beta = 3$. In the table, we also show the results for $\langle D \rangle$, for $\langle \Delta N \rangle / \tilde{L}$ and for $\langle \Delta E \rangle / L$, which are the angular averages of $D(\theta, \phi)$, $\Delta N(\theta, \phi)/\tilde{L}$ and $\Delta E(\theta, \phi)/L$, respectively. We notice that $|\langle \Delta N \rangle|/\tilde{L} \ll 0.5$ when $\tilde{L} \sim 10^3$, which confirms the inadequacy of using symmetric vortex–lattice configurations when evaluating the mesoscopic pinning force (Jones 1990).

From these results, it is possible to see that there is a strong dependence of the pinning force per unit length on the parameter L: increasing the length of the vortex, a consistent decrease in the mesoscopic pinning force can be observed. This behaviour was indeed expected, following the argument by Jones (1991) that the difference in energy between adjacent configurations becomes vanishingly small for infinite vortex rigidity ($L \to \infty$). However, using a realistic vortex length of order $\sim 10^3 R_{\text{ws}}$, as discussed in Section 2.3, the pinning force is still not negligible.

The other important parameter of the model is the polarization factor β. The results show that f_L does not depend very strongly on the choice of this parameter in the three lower density regions, while the effect is more important in the two high-density regions, where the mesoscopic pinning force is significantly larger in the strong pairing scenario ($\beta = 1$) than in the weak one ($\beta = 3$). It is also

Table 3. Results of the calculations for vortices with length L up to 5000 R_{ws}. The parameters of Table 2 were used as inputs for the counting procedure. The quantities $\langle D \rangle$, $\langle \Delta N \rangle / \tilde{L}$ and $\langle \Delta E \rangle / L$ are the angular averages of $D(\theta, \phi)$, $\Delta N(\theta, \phi) / \tilde{L}$ and $\Delta E(\theta, \phi) / L$, respectively. The last two columns show the force per unit length and its uncertainty.

L (R_{ws})	β	No.	r_c (R_{ws})	$\langle D \rangle$ (R_{ws})	$\langle \Delta N \rangle / \tilde{L}$ (10^{-2})	$\langle \Delta E \rangle / L$ (10^4 erg cm^{-1})	f_L (10^{15} dyn cm^{-1})	σ_{f_L} (10^{15} dyn cm^{-1})
100	1	1	0.289	1.320	4.185	0.549	1.222	0.086
		2	0.313	1.356	4.466	1.290	3.404	0.250
		3	0.204	1.270	−3.687	5.689	22.970	1.453
		4	0.531	2.064	−5.994	17.127	61.521	5.689
		5	2.514	3.893	−13.779	5.439	12.578	2.501
	3	1	0.591	2.072	6.730	0.417	0.630	0.069
		2	0.555	2.005	6.496	0.704	1.362	0.143
		3	0.504	2.060	−5.866	7.240	18.459	1.751
		4	1.490	3.396	−9.725	5.542	10.904	1.698
		5	8.080	4.634	−23.797	0.553	0.994	0.256
500	1	1	0.289	2.066	1.940	0.254	0.367	0.058
		2	0.313	2.142	2.031	0.587	1.015	0.167
		3	0.204	1.732	−1.504	2.321	7.190	0.833
		4	0.531	2.880	−2.342	6.693	17.690	3.028
		5	2.514	4.348	−5.184	2.046	4.349	1.277
	3	1	0.591	3.092	2.900	0.179	0.191	0.046
		2	0.555	2.970	2.809	0.304	0.416	0.095
		3	0.504	2.804	−2.305	2.845	5.418	0.946
		4	1.490	3.915	−3.541	2.018	3.529	0.726
		5	8.080	4.842	−8.812	0.205	0.375	0.130
1000	1	1	0.289	2.407	1.431	0.188	0.238	0.053
		2	0.313	2.467	1.491	0.431	0.651	0.152
		3	0.204	2.049	−1.086	1.676	4.388	0.744
		4	0.531	3.210	−1.615	4.616	11.033	2.587
		5	2.514	4.467	−3.575	1.411	3.024	1.090
	3	1	0.591	3.358	2.113	0.131	0.133	0.042
		2	0.555	3.283	2.044	0.221	0.286	0.088
		3	0.504	3.129	−1.606	1.982	3.403	0.816
		4	1.490	4.131	−2.362	1.346	2.350	0.566
		5	8.080	4.938	−6.037	0.140	0.267	0.112
2500	1	1	0.289	2.845	1.031	0.135	0.149	0.050
		2	0.313	2.900	1.067	0.308	0.420	0.143
		3	0.204	2.533	−0.756	1.167	2.462	0.688
		4	0.531	3.544	−1.062	3.034	6.777	2.324
		5	2.514	4.648	−2.355	0.930	2.184	0.981
	3	1	0.591	3.663	1.513	0.094	0.096	0.040
		2	0.555	3.530	1.455	0.158	0.207	0.083
		3	0.504	3.468	−1.074	1.325	2.205	0.740
		4	1.490	4.294	−1.463	0.833	1.506	0.466
		5	8.080	4.992	−3.941	0.092	0.190	0.101
5000	1	1	0.289	3.067	0.852	0.112	0.123	0.049
		2	0.313	3.147	0.884	0.255	0.339	0.140
		3	0.204	2.783	−0.603	0.930	1.828	0.656
		4	0.531	3.731	−0.828	2.366	5.317	2.233
		5	2.514	4.681	−1.834	0.724	1.801	0.936
	3	1	0.591	3.799	1.223	0.076	0.080	0.039
		2	0.555	3.714	1.183	0.128	0.171	0.080
		3	0.504	3.632	−0.844	1.042	1.677	0.713
		4	1.490	4.482	−1.085	0.618	1.133	0.433
		5	8.080	5.044	−2.996	0.070	0.153	0.096

worth noting that changing the polarization factor from $\beta = 1$ to 3 results in a shift to lower densities of the maximum of the pinning profile. The position in density of the maximum pinning force can be relevant to determine the angular momentum accumulated in the crust between pulsar glitches, as discussed in Pizzochero (2011).

A comparison between our results and those found in the literature shows that the maximum pinning forces per unit length obtained in this work are at least two orders of magnitude smaller than those found for an aligned vortex (Anderson et al. 1982; Alpar et al. 1984a) and which have been commonly used in the study
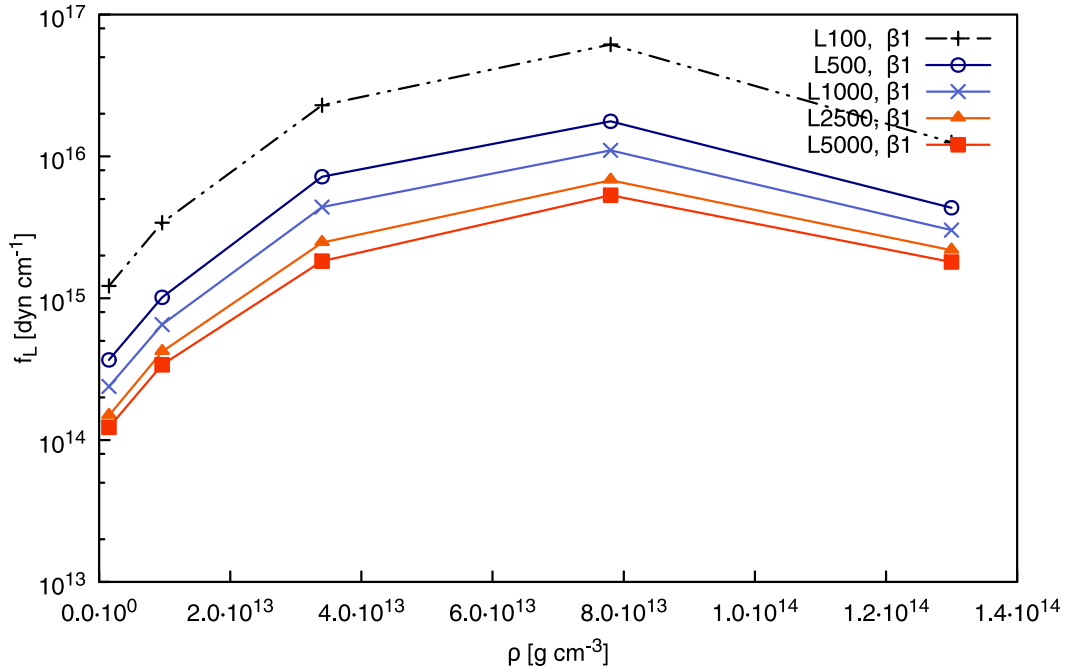
Figure 10. The pinning force per unit length for the $\beta = 1$ case. The mesoscopic pinning force is plotted as a function of the baryonic density of matter for the five zones considered and for different vortex lengths.
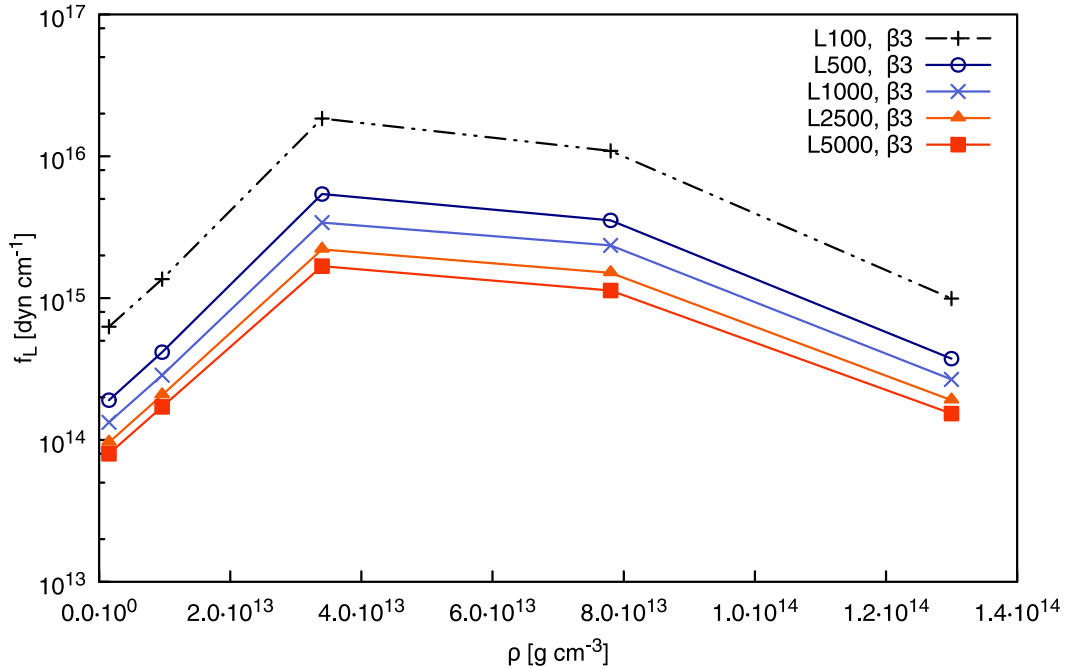

Figure 11. The pinning force per unit length for the $\beta = 3$ case. The pinning force per unit length for the $\beta = 1$ case. The mesoscopic pinning force is plotted as a function of the baryonic density of matter for the five zones considered and for different vortex lengths.

of pulsar glitches. Our results are also about one order of magnitude smaller than those obtained by Link (2014) with a variational approach. Note that the main contribution to this difference derives from our estimate of the separation between pinned configurations, obtained from the counting procedure described above, which is larger than that used by Link (2014). As we shall discuss in the following, however, the forces we calculate are still large enough to account for the large glitches observed in the Vela pulsar.

Finally, our calculations also provide an estimate of the fluctuations in local pinning strength that may be possible. The results in Table 3 show that such fluctuations are generally of the order
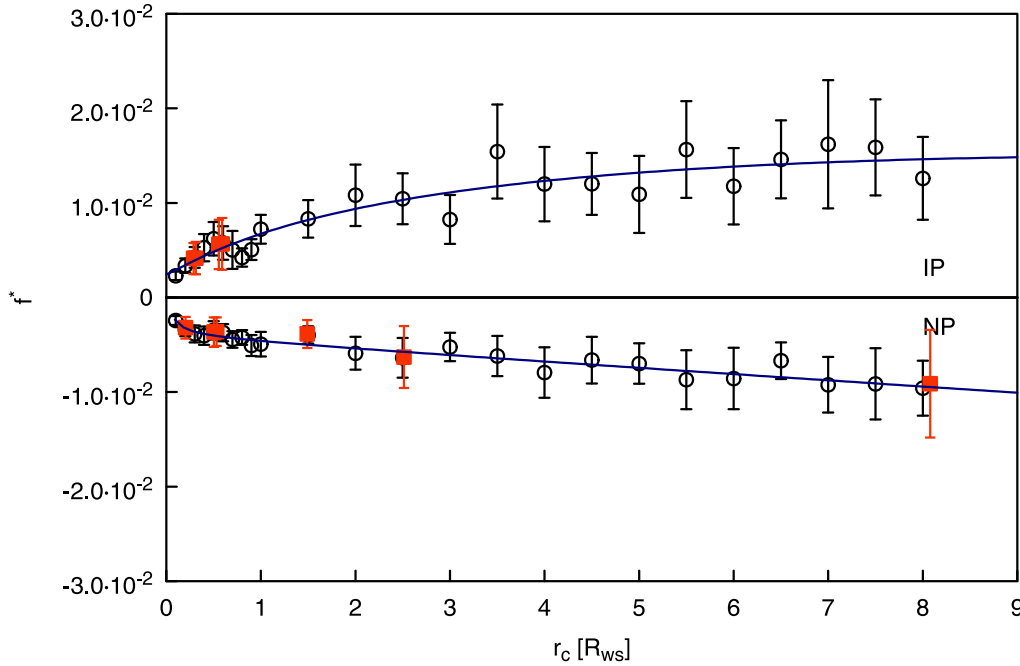
Figure 12. Plot of the calculated values of $\tilde{f}_{\tilde{L}}$ (for $\tilde{L} = 5000$) as a function of the capture radius r_c (in units of R_{ws}). The error bars for the estimated errors on $\tilde{f}_{\tilde{L}}$ are also shown. The red squares are the values of $\tilde{f}_{\tilde{L}}$ corresponding to the 10 values of r_c in Table 2. The fitting curves f^* for both the IP (above) and NP (below) regimes are also shown (see Table 4).

of ≈ 10 per cent of the pinning force, but can be larger in weaker pinning regions.

4.1 Analytic approximations

The results presented up to now refer to the calculation of the mesoscopic pinning force corresponding to the fiducial parameters R_{ws}, R_N, ξ and E_p in Table 1. However, existing or future calculations of the inner crust nuclear structure, of the neutron superfluid pairing properties and of the microscopic vortex–nucleus interaction may provide alternative sets of parameters to those used in the present work. It is possible to generalize our approach and obtain a simple analytic expression which allows us to calculate the pinning force per unit length f_L for different choices of the input parameters.

In equation (20), the quantity E_{eff} can be factorized. We can also express all the lengths in R_{ws} units and then define an adimensional quantity $\tilde{f}_{\tilde{L}}(\tilde{r}_c)$ that depends *only* on the adimensional capture radius $\tilde{r}_c = r_c/R_{ws}$ and the adimensional vortex length $\tilde{L} = L/R_{ws}$. The quantity $\tilde{f}_{\tilde{L}}(\tilde{r}_c)$ is purely geometrical and it contains all the information obtained from the counting procedure described in the preceding sections. The force per unit length f_L can then be obtained as

$$f_L = \tilde{f}_{\tilde{L}}(\tilde{r}_c) \frac{E_{\text{eff}}}{R_{ws}^2}. \qquad (21)$$

We have calculated $\tilde{f}_{\tilde{L}}(\tilde{r}_c)$ for different choices of $\tilde{r}_c$ (in the realistic range 0–8) and for different vortex lengths (of the order of $\tilde{L} \sim 10^3$) for both the NP and IP regimes. We then fitted a non-linear function $f^*(x)$ to the calculated values of $\tilde{f}_{\tilde{L}}$: we used a function of the form

$$f^*(x) = Ax + B \left[\log(1+x)\right]^W + C, \qquad (22)$$

where A, B, C and W are the parameters to be fitted. In Fig. 12, we show the results for the $\tilde{L} = 5000$ case; the error bars have also been

Table 4. Fit parameters for the function $f^*(x) = Ax + B \left[\log(1+x)\right]^W + C$. Three different vortex lengths L are considered for both the NP and IP regimes.

		A (10^{-3})	B (10^{-3})	W	C (10^{-3})
$L = 1000 R_{ws}$	NP	−0.315	−1.296	1.974	−7.298
	IP	−2.099	9.043	1.586	7.212
$L = 2500 R_{ws}$	NP	−0.755	1.119	−0.366	−6.209
	IP	−0.374	7.685	0.997	3.057
$L = 5000 R_{ws}$	NP	−0.646	0.466	−0.643	−4.529
	IP	−0.772	7.641	1.114	2.428

added, as obtained from the propagation of the error on $n_{\text{bound}}(\theta, \phi)$. We see that the calculated points can be fitted reasonably (within the error bars) with the choice of parametrization in equation (22). In Table 4, we give the parameters obtained from the fitting procedure.

We notice that, within the uncertainty given by the quite large error bars, there is no significant difference in the magnitude of $\tilde{f}_{\tilde{L}}(\tilde{r}_c)$ between the *nuclear* and the *interstitial* regime. This means that the force per unit length, for given $\tilde{r}_c$ and E_{eff}, remains roughly the same if we take the microscopic vortex–nucleus force to be attractive or repulsive. The fact that attractive and repulsive vortex–nucleus interactions are equivalent for the pinning of vortices to the lattice was already noted by Link (2009).

4.2 Vortex length

As discussed in Section 2.3, the parameter L depends on the vortex tension, according to equation (15). The tension T can be expressed as (Thomson 1880; Fetter 1967; Andersson et al. 2007)

$$T = \rho_n \frac{\kappa^2}{4\pi} \log\left(\frac{a}{\xi}\right), \qquad (23)$$

Table 5. Fitting results for the pinning force per unit length as a function of the vortex length L, for the five crustal zones (see the text for details). The table reports also the best estimate for L and the corresponding calculated value of f_L.

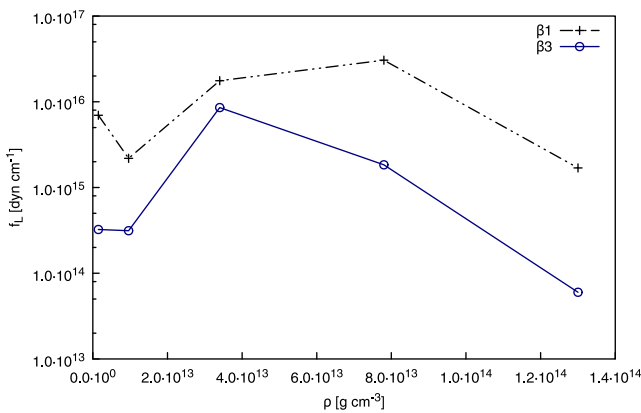| β	No.	G (10^{19} dyn cm^{-1})	H	L (R_{ws})	f_L (10^{16} dyn cm^{-1})
$\beta = 1$	1	0.052	−3.968	20	0.695
	2	0.151	−3.990	171	0.220
	3	1.086	−4.033	137	1.763
	4	3.527	−4.159	232	3.055
	5	0.228	−3.409	3984	0.169
$\beta = 3$	1	0.019	−3.740	244	0.032
	2	0.041	−3.739	913	0.031
	3	0.925	−4.071	260	0.855
	4	0.335	−3.751	1634	0.184
	5	0.013	−3.173	69 726	0.006

Figure 13. Plot of the values of pinning force per unit length reported in Table 5. These results are obtained by performing a fit for the dependence of f_L on the rigidity length L of the vortex (for each of the five zones considered), and then using equations (15) and (23).

where $\kappa = \pi\hbar/m_{\mathrm{n}}$ is the quantum of circulation, a is the inter-vortex spacing and the neutron density is given by $\rho_{\mathrm{n}} = x_{\mathrm{n}}\rho$ with the neutron fraction $x_{\mathrm{n}} \approx 0.9$–0.95 (Zuo et al. 2004). Given the logarithmic dependence on these parameters, we choose to expedite calculations and follow Andersson et al. (2007) and take a constant value for the quantity $x_{\mathrm{n}}\log(a/\xi) = 20$ [note that a smaller value is considered by Link (2014)]. For each zone of the crust, we calculate the tension and estimate the length L over which we can consider the vortex as rigid. The dependence of the pinning force f_L on the parameter L is obtained by fitting, for every configuration (β, zone #) considered in Table 3, a function of the form

$$f = G \left[\log(L/R_{\mathrm{ws}}) \right]^H, \tag{24}$$

where G and H are the parameters to be fitted. In Table 5, we report the results of the fit, together with the values of the vortex length L: we can see that at lower densities the vortex is less rigid, with a significant enhancement in the rigidity taking place at high densities. The last column refers to the final result for the pinning force per unit length obtained by using the calculated value for L. These values are also plotted in Fig. 13: the dashed line refers to the $\beta = 1$ condition, while the solid one is obtained with $\beta = 3$, which is a more realistic case, as indicated also by the results of Gandolfi et al. (2008). Although the variable tension changes the profile of pinning with density as compared to the case with constant tension, the mesoscopic pinning force still has values in the range
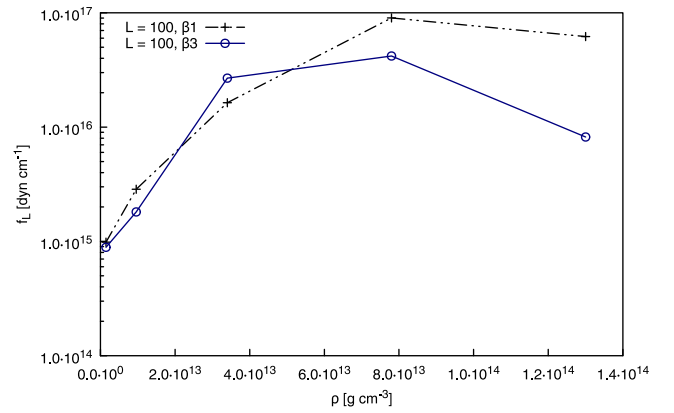

Figure 14. The pinning force per unit length for the $\beta = 1$ and 3 case for a random lattice configuration. The mesoscopic pinning force is plotted as a function of the baryonic density of matter for the five zones considered. These results are referred to a vortex of length $L = 100\,R_{\mathrm{ws}}$. The order of magnitude of the pinning force is the same as in the BCC configuration.

$f_L \approx 10^{14}$–10^{15} dyn cm^{-1} for the realistic choice $\beta = 3$, while the largest densities (zone 5) correspond to superweak pinning (Alpar et al. 1984a).

5 RESULTS OF THE MODEL: RANDOM LATTICE

Given the uncertainties on the state of the crust at high densities, and the possibility that it may form a much less ordered structure than a BCC lattice (Kobyakov & Pethick 2014), let us consider the case of a random lattice, analogous to the case considered by Link (2009).

The pinning force for a random lattice is calculated by applying the same procedure described for the BCC configuration. We consider a vortex of length L inside a box of side $L + l$, where l defines the area on which we perform the parallel-transport operation, as done previously. As we intend to compare the results from the BCC configuration with this new setup, the box which represents our lattice must be filled with an adequate number N_{p} of sites in order to obtain the same density. In a BCC lattice with Wigner–Sietz cells of radius R_{ws}, the density of pinning sites is $n_{\mathrm{p}} = 1/(4R_{\mathrm{ws}}^3)$ and therefore the number of points we include in the random lattice, for comparison, must be

$$N_{\mathrm{p}} = \frac{(L+l)^3}{4R_{\mathrm{ws}}^3}. \tag{25}$$

The lattice is constructed by generating N_{p} points extracted from a uniform distribution inside the box. For each orientation (θ, ϕ) of the vortex, we parallel-transport it, and for each position we count the number of sites that fall inside the capture radius, as described previously, in order to evaluate the pinning force per unit length $F_L(\theta, \phi)$. Once we have generated a random lattice, we keep it fixed for all orientations of the vortex.

The results for the different zones are shown in Fig. 14. We can see that in general the order of magnitude of the pinning force is the same as in the BCC case, and appears to be determined by the average distance between pinning sites, the pinning energy, the coherence radius of the vortex and its rigidity at a given density, with the exact nature of the lattice only contributing a geometrical factor of order unity. Note that for a random lattice the distance between nuclei is, obviously, much more variable than for an ordered lattice,

which will increase the error on our estimate of the bending length-scale L. However, given the scaling of the pinning force as $f_L \sim 1/\sqrt{L}$, upon averaging we still expect an error of less than a factor of a few in our estimates of the force itself.

The results presented here can also be explained by simple analytic considerations which involve Poisson statistics. For a random lattice configuration, the average density of pinning sites is simply $n_N \approx 1/R_{ws}^3$ and therefore the number of sites inside a cylinder of radius r_c and length L is

$$N \approx \frac{Lr_c^2}{R_{ws}^3}. \qquad (26)$$

The numerical calculations presented above suggest that the typical distance D between two maximal pinning configuration is of the order of R_{ws}, so we can estimate the force per unit length as $f_L = \Delta N E_{eff}/(L R_{ws})$, with typical fluctuations in number of counted sites of $\Delta N = \sqrt{N}$ as we are considering a Poisson distribution. The final result is

$$f_L = \frac{1}{L}\frac{E_{eff}}{R_{ws}}\frac{r_c}{R_{ws}}\sqrt{\frac{L}{R_{ws}}} = \frac{E_{eff}}{R_{ws}^2}\frac{\tilde{r}_c}{\sqrt{\tilde{L}}} = f^*\frac{E_{eff}}{R_{ws}^2}. \qquad (27)$$

For $\tilde{r}_c \sim 1$ and $\tilde{L} \sim 10^3$, we obtain a reduction factor $f^* \sim 10^{-2}$ in agreement with the results of the previous sections.

Note also that the previous estimate for the pinning length has the same functional dependence on L, and thus on the tension, as the results of Link (2012). We can thus interpret the average separation between pinning sites, l_p, introduced by Link & Cutler (2002) and Link (2012) in our scheme. In our case, l_p represents the average distance between the additional 'extra' pinning sites ΔN that lead to the difference between the bound and free energy configurations, namely $\tilde{l}_p = l_p/R_{ws}$ is the inverse of the quantity $\langle \Delta N \rangle / \tilde{L}$ shown in Table 3. We remind the reader, however, that the vortex is never completely free from pinning sites and our 'free' configuration also contains pinning sites. The distance l_p must thus be interpreted as a 'virtual' quantity between the ΔN excess pinning sites. As already discussed in Section 2.3, it is not the actual distance between physical nuclei, as in practice the average distance between NP sites is always of the order of R_{ws}.

6 APPLICATION TO PULSAR GLITCHES

Let us briefly outline how our results can impact on models of pulsar glitches. Let us consider a single pinned vortex: the forces acting on a section of it will be the pinning force calculated above $f_L(\rho)$ and the Magnus force $f_M = \kappa \rho_n \hat{\Omega} \times (v_n - v_v)$, where $\hat{\Omega}$ is a unit vector along the rotation axis, ρ_n is the density of superfluid neutrons and v_n and v_v are the velocities of the superfluid neutrons and of the vortices, respectively. Integrating these two contributions over the full length of the vortex (which is taken to be straight), balancing them and assuming that the pinned vortices move with the crust, allows us to determine, as a function of the distance from the rotational axis of the star, the *critical lag* for unpinning $\Delta\Omega_c = \Omega_n - \Omega_p$, with Ω_p the angular velocity of the crust (the one which is observed). In Fig. 15, we show an example of the radial profile $\Delta\Omega_c$ for a typical $1.4\,M_\odot$ NS, with the GM1 equation of state as detailed in Seveso, Pizzochero & Haskell (2012). We can then follow the prescription of the 'snowplough' model of Pizzochero (2011), and assume that as a pulsar spins down, vortices move out of the core and inner crust, and repin in the strong pinning region, eventually forming a vortex sheet close to the maximum $\Delta\Omega_{c_{max}}$ of the critical lag. Given an equation of state and a critical unpinning

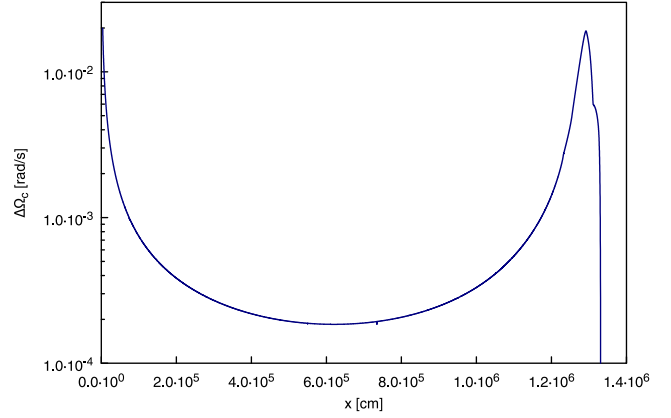**Figure 15.** Critical unpinning lag $\Delta\Omega_c$ of an NS of $1.4\,M_\odot$. This profile has been obtained with a realistic model, by solving the general relativistic TOV equations and using the GM1 equation of state, as detailed in Seveso et al. (2012).

profile, we can therefore calculate the number of vortices involved in the process and the angular momentum stored by them, which eventually will power the glitch. It is also easy to evaluate the expected waiting time between glitches, that is the time needed to build the maximum critical lag:

$$t_{gl} = \frac{\Delta\Omega_{c_{max}}}{|\dot{\Omega}_p|}, \qquad (28)$$

where $\dot{\Omega}_p$ is the observed pulsar spin-down rate and for the moment we neglect effects of superfluid entrainment.

Following the approach of Pizzochero (2011), we can then compare the results of the present work to the giant glitches of the Vela pulsar: we find that, for example, a typical observed glitch size of $\delta\Omega_p/\Omega_p \approx 10^{-6}$ can be obtained for a star of mass $1.3\,M_\odot$ with the GM1 equation of state, using the mesoscopic pinning force corresponding to $L = 5000\,R_{ws}$ and $\beta = 3$. It is also worth noting that equation (28) gives for Vela a waiting time of ~ 3 yr (in agreement with observational data), when the maximum of the mesoscopic pinning force is $f_{max} \approx 10^{15}$ dyn cm^{-1} (as is the case for $L = 5000\,R_{ws}$ and $\beta = 3$). A more detailed study of the dependence of the snowplough model on parameters such as the equation of state and the mass of the star can be found in Seveso et al. (2012) and Haskell, Pizzochero & Seveso (2013). Effects of superfluid entrainment will also be considered in future work, as strong entrainment in the crust can severely limit the amount of angular momentum that is exchanged during a glitch and allow one to set constraints on the equation of state (Andersson et al. 2012; Chamel 2013; Newton, Berger & Haskell 2015).

The simple model above shows that the pinning profiles we have calculated can play a very important role in the study of glitches, and could be used as a background for more realistic glitch models and vortex dynamics simulations (Peralta et al. 2006; Warszawski & Melatos 2008, 2011; Sidery, Passamonti & Andersson 2010; Haskell, Pizzochero & Sidery 2012; Haskell & Antonopoulou 2014). Note that here we have only calculated the contribution to the pinning force acting on a vortex from the ions in the crust. In the core of the NS, however, protons are expected to form a type II superconductor, in which the magnetic field is organized in flux tubes, that can interact strongly and 'pin' the vortices (Haskell et al. 2013). We intend to apply the procedure described above to this scenario in a subsequent paper.

7 CONCLUSIONS

In this paper, we present a calculation of the pinning force per unit length acting on a vortex in an NS crust. We have calculated the mesoscopic pinning force at different densities for straight vortices that cross the star inner crust, and averaged over all the possible orientations of the crustal lattice with respect to the vortex. Our results confirm the expectations of Jones (1991), that the averaging procedure over different orientations tends to smooth out energy differences between different configurations, leading to weaker pinning forces. In the limit of infinitely long vortices, the pinning force would vanish; for realistic values of the vortex tension and for the realistic choice $\beta = 3$, however, the force per unit length is still sizeable and in the range $f_L \approx 10^{14}$–10^{15} dyn cm^{-1} depending on the position in the crust. These values are significantly smaller than those found in the literature; for instance, Link (2014) obtains values typically of the order of $f_L \approx 10^{16}$ dyn cm^{-1}. We find that the mesoscopic pinning force depends very little on whether the pinning force is attractive (NP) or repulsive (IP) in a given region of the star, but it can be quite sensitive to in-medium polarization effects, which can shift the position of the maximum and thus alter the angular momentum distribution in the crust of an NS. Furthermore, we have also considered the case of a more disordered crystal configuration than a BCC lattice and studied a random lattice. In this case, the pinning force does not vary significantly from the estimates in the BCC case, and depends mainly on the average distance between pinning sites, the pinning energy, the coherence length and rigidity of the vortex, with the exact nature of the lattice only contributing a geometric factor of order unity.

We also apply the calculated forces to the problem of pulsar glitches and show how, in the framework of the 'snowplough' model (Pizzochero 2011), our results can explain large glitches in the Vela pulsar. More generally, the forces that we calculate can be used to generate realistic pinning profiles for glitch models (Haskell et al. 2012, Haskell & Antonopoulou 2014), simulations of vortex dynamics in NSs (Warszawski & Melatos 2008) or mode calculations (Glampedakis & Andersson 2009; Link 2012). Future work will aim to include consistently the effect of strong crustal entrainment, as Link (2014) has shown that including entrainment phenomenologically by rescaling the free neutron density can have important consequences for vortex creep, and more generally strong entrainment provides strong constraints for glitch models (Andersson et al. 2012; Chamel 2013).

Finally, let us note that we have considered the case of straight vortices that cross the star. Although this is the natural starting point for such a calculation, in a realistic NS the vortex array is likely to form a turbulent tangle (see e.g. Andersson et al. 2007) and pinning can also occur between vortices and superconducting flux tubes in the outer core of the NS, leading not only to an increased reservoir of angular momentum, but also to a modified response of the star to a glitch (Sidery & Alpar 2009; Haskell et al. 2013; Gügercinoğlu & Alpar 2014). Such configurations have a different topology from the one considered in this paper, and the behaviour of the pinning force in these cases is not captured by our current approach. In principle, our calculation can, however, be modified to account for them. Furthermore, as already mentioned, the crust of an NS may not form a BCC lattice but may exhibit a much more inhomogeneous structure (Kobyakov & Pethick 2014) or exhibit several kinds of 'pasta' phases at the crust/core interface (Lorenz, Ravenhall & Pethick 1970), altering the geometry of the nuclear clusters. We intend to explore in detail the consequences of these effects on vortex pinning in future work.

Finally, we note that our approach relies on calculating energy differences between vortex configurations and deriving from them a pinning force per unit length; therefore, it cannot give any information about the short-range radial profiles of the mesoscopic pinning energies and forces (incidentally, the existing microscopic studies of the vortex–nucleus interaction are also based on energy arguments between specific configurations, giving no information about the short-range radial dependence of the interaction). Dynamical vortex line simulations will thus be necessary to assess the stability of these configurations and how vortices move from one to another.

ACKNOWLEDGEMENTS

REFERENCES

Alpar M. A., 1977, ApJ, 213, 527
Alpar M. A., Pines D., Anderson P. W., Shaham J., 1984a, ApJ, 276, 325
Alpar M. A., Anderson P. W., Pines D., Shaham J., 1984b, ApJ, 278, 791
Alpar M. A., Chau H. F., Cheng K. S., Pines D., 1994, ApJ, 427, L29
Alpar M. A., Chau H. F., Cheng K. S., Pines D., 1996, ApJ, 459, 706
Anderson P. W., Itoh N., 1975, Nature, 256, 25
Anderson P. W., Alpar M. A., Pines D., Shaham J., 1982, Phil. Mag. A, 45, 227
Andersson N., Sidery T., Comer G. L., 2007, MNRAS, 381, 747
Andersson N., Glampedakis K., Ho W. C. G., Espinoza C. M., 2012, Phys. Rev. Lett., 109, 241103
Baym G., Pethick C., Pines D., Ruderman M., 1969, Nature, 224, 872
Bildsten L., 1998, ApJ, 501, L89
Chamel N., 2012, Phys. Rev. C, 85, 035801
Chamel N., 2013, Phys. Rev. Lett., 110, 011101
Donati P., Pizzochero P. M., 2003, Phys. Rev. Lett., 90, 21
Donati P., Pizzochero P. M., 2004, Nucl. Phys. A, 742, 363
Donati P., Pizzochero P. M., 2006, Phys. Lett. B, 640, 74
Elshamouty K. G., Heinke C. O., Sivakoff G. R., Ho W. C. G., Shternin P. S., Yakovlev D. G., Patnaude D. J., David L., 2013, ApJ, 777, 22
Epstein R. I., Baym G., 1988, ApJ, 328, 680
Espinoza C. M., Lyne A. G., Stappers B. W., Kramer M., 2011, MNRAS, 414, 1679
Fetter A. L., 1967, Phys. Rev. D, 4, 1589
Gandolfi S., Illarionov A. Yu., Fantoni S., Pederiva F., Schmidt K. E., 2008, Phys. Rev. Lett., 101, 132501
Glampedakis K., Andersson N., 2009, Phys. Rev. Lett., 102, 141101
Gudmundsson E. H., Pethick C. J., Epstein R. I., 1983, ApJ, 272, 286
Gügercinoğlu E., Alpar M. A., 2014, ApJ, 788, L11
Haskell B., Melatos A., 2015a, International J. Modern Phy. D, 24, 1530008
Haskell B., Melatos A., 2015b, MNRAS, submitted, preprint (arXiv:1510.03136)
Haskell B., Pizzochero P. M., Sidery T., 2012, MNRAS, 420, 658
Haskell B., Pizzochero P. M., Seveso S., 2013, ApJ, 746 L25
Haskell B., Antonopoulou D., 2014, MNRAS, 438, L16
Hirasawa M., Shibazaki N., 2001, ApJ, 563, 267
Jones P. B., 1990, MNRAS, 243, 257
Jones P. B., 1991, ApJ, 373, 208
Kobyakov D., Pethick C., 2014, Phys. Rev. Lett., 112, 112504
Link B., 2009, Phys. Rev. Lett., 102, 131101
Link B., 2012, MNRAS, 422, 1640
Link B., 2014, MNRAS, 789, 141
Link B., Cutler C., 2002, MNRAS, 336, 211

Lorenz C. P., Ravenhall D. G., Pethick C. J., 1993, Phys. Rev. Lett., 70, 379

Middleditch J., Marshall F. E., Wang Q. D., Gotthelf E. V., Zhang W., 2006, ApJ, 625, 1531

Migdal A. B., 1959, ApJ, 743, L20

Negele J. W., Vautherin D., 1973, Nucl. Phys. A, 207, 298

Newton W. G., Berger S., Haskell B., 2015, MNRAS, 454, 4400

Page D., Parakash M., Lattimer J. M., Steiner A. W., 2011, Phys. Rev. Lett., 106, 081101

Peralta C., Melatos A., Giacobello M., Ooi A., 2005, ApJ, 635, 1224

Peralta C., Melatos A., Giacobello M., Ooi A., 2006, ApJ, 651, 1079

Piekarewicz J., Fattoyev F. J., Horowitz C. J., 2014, Phys. Rev. C, 90, 015803

Pizzochero P. M., 2011, ApJ, 743, L20

Ruderman M., 1969, Nature, 223, 597

Ruderman M., 1976, ApJ, 203, 213

Sedrakian A. D., 1995, MNRAS, 277, 225

Seveso S., Pizzochero P. M., Haskell B., 2012, MNRAS, 427, 1089

Shternin P. S., Yakovlev D. G., Heinke C. O., Ho W. C. G., Patnaude D. J., 2011, MNRAS, 412, L108

Sidery T., Alpar M. A., 2009, MNRAS, 400, 1859

Sidery T., Passamonti A., Andersson N., 2010, MNRAS, 405, 1061

Steiner A. W., Gandolfi S., Fattoyev F. J., Newton W. G., 2014, Phys. Rev. C, 91, 015804

Thompson C., Duncan R. C., 1995, MNRAS, 275, 255

Thomson W., 1880, Phil. Mag., 10, 155

Warszawski L., Melatos A., 2008, MNRAS, 390, 175

Warszawski L., Melatos A., 2011, MNRAS, 415, 1611

Warszawski L., Melatos A., 2013, MNRAS, 428, 1911

Zuo W., Li Z. H., Lu G. C., Li J. Q., Scheid W., Lombardo U., Schulze H.-J., Shen C. W., 2004, Phys. Lett. B, 595, 44

APPENDIX A: VORTEX RIGIDITY AND UNPINNING

Let us begin by writing the equations of motion for a single vortex. The forces acting on a vortex will be the Magnus force:

$$f_M^i = \kappa \rho_n \epsilon^{ijk} \hat{k}_j (v_k^L - v_k^n), \tag{A1}$$

and the non-dissipative part of the interaction with the pinning site, i.e. the 'pinning' force F_p^i. For simplicity, we neglect mutual friction in this example. The equations of motion for a vortex thus take the form

$$\epsilon^{ijk} \hat{k}_j (v_k^L - v_k^n) + \mathcal{F}_p^i = 0, \tag{A2}$$

where v_i^L is the velocity of the vortex line and v_i^n is the velocity of the superfluid neutrons, ρ_n the superfluid neutron mass density and $\mathcal{F}_p^i = F_p^i/\rho_n\kappa$, with κ the quantum of circulation (and $\hat{k}_i$ the unit vector along the vorticity axis, taken to be the z-axis in the following).

As already discussed, the large self-energy of a vortex leads to tension due to flow around a curved segment, which introduces additional components in the individual neutron velocities, of the form (Andersson et al. 2007)

$$\delta v_i^n = \gamma_n(\varepsilon) \nu \epsilon_{ijk} \hat{k}^j \hat{k}^p \nabla_p \hat{k}^k, \tag{A3}$$

where γ is a function of the entrainment parameter ε and

$$\nu = \frac{\kappa}{4\pi} \log\left(\frac{a}{\xi}\right) \tag{A4}$$

with a the inter vortex spacing and ξ the coherence length associated with the vortex core, so that one has

$$\log\left(\frac{a}{\xi}\right) \approx 20 - \frac{1}{2}\log\left(\frac{\Omega_n}{100\,\text{rad s}^{-1}}\right) \tag{A5}$$

which, as discussed in the main text, is essentially a constant for the range of periods of interest. Equation (23) shows that the tension is $T = \nu\kappa\rho_n$. It is thus sufficient to add the contributions in equation (A3) to the general flows in equation (A2).

For simplicity, we follow Sedrakian (1995) and take a parabolic pinning potential U_p of the form[2]

$$U_p = \frac{1}{2}A(r_i r^i - r_0^i r_{0i}) \quad \text{for } |r_i r^i - r_0^i r_{0i}| \leq R_{\text{range}} \tag{A6}$$

$$U_p = 0 \quad \text{for } |r_i r^i - r_0^i r_{0i}| > R_{\text{range}} \tag{A7}$$

so that the pinning force $F_p^i = -\nabla^i U_p$ takes the form

$$F_p^i = -A(r^i - r_0^i) \quad \text{for } |r_i r^i - r_0^i r_{0i}| \leq R_{\text{range}} \tag{A8}$$

$$F_p^i = 0 \quad \text{for } |r_i r^i - r_0^i r_{0i}| > R_{\text{range}}, \tag{A9}$$

where A is a constant that describes the strength of the interaction and r_0^i is the position of the pinning site, which for simplicity we shall take at the origin in the following, i.e. $r_0^i = 0$.

Consider a pinned vortex that has to bend to free itself from one pinning bond. We work in a frame comoving with the protons and take the background neutron velocity to be in the y direction. To simplify our treatment, we also assume that as a vortex moves out in the x direction, driven by the Magnus force, it will take the shape of an ellipse in the x–z plane, as depicted in Fig. A1, where b is the distance from the centre of the pinning site on the x-axis and L is the length over which the vortex bends in the z direction. Consider first a vortex that has unzipped from a single pinning site, so that $b \approx R_{\text{range}}$. The equations of motion for the vortex take the form

$$v_i^L = V_i^n + \epsilon_{ijk} \hat{k}^j \mathcal{F}^k - \hat{k}_i \hat{k}^j V_j^n + \gamma_n(\varepsilon) \nu \epsilon_{ijk} \hat{k}^j \hat{k}^p \nabla_p \hat{k}^k, \tag{A10}$$

where we have indicated as V_i^n the *background* superfluid neutron velocity (without the curvature induced contributions), and we take $\gamma_n = 1$ [which is appropriate in the crust for strong entrainment; see Haskell & Melatos (2015b) and Chamel (2012)]. Given that $\hat{k}_i$ has components only in the x–z plane, it is sufficient to consider the vortex line velocity in the x direction:

$$v_y^L = V_y^n + (\hat{k}^z \mathcal{F}^x - \hat{k}^x \mathcal{F}^z) + \nu[\hat{k}^z \hat{k}_p \nabla^p \hat{k}_x - \hat{k}^x \hat{k}_p \nabla^p \hat{k}_z] \tag{A11}$$

which, evaluated at $z = 0$ and at a point $x = b$ for the configuration in Fig. A1, leads to

$$v_y^L = V_y^n - \mathcal{A}b - \nu\frac{b}{L^2}, \tag{A12}$$

where $\mathcal{A} = A/(\kappa\rho_n)$. Equation (A12) shows that the tension acts in the same direction of the pinning force and tends to maintain the vortex straight. The critical velocity $\bar{V}_{cT}$ for unpinning with tension, compared to the critical velocity V_{cr} in the absence of tension, is thus

$$\bar{V}_{cT} = V_{cr} + \frac{\nu R_{\text{range}}}{L^2}, \tag{A13}$$

where R_{range} is the range of the pinning potential. Bending, and thus unpinning, over the length-scale of a single bond is essentially prohibited by the tension, since taking $L \approx R_{\text{range}} \approx R_{ws}$ leads to critical velocities of the order of $\bar{V}_{cT} \approx 10^8$ cm s^{-1}, far greater than

[2] As already noted, to date the short-range radial dependence of the vortex–nucleus interaction is not known.
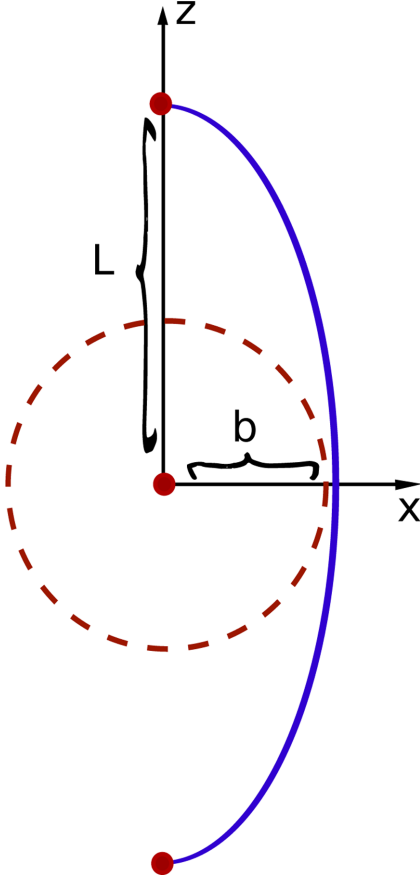
Figure A1. A schematic (out of scale) representation of a curved vortex, pinned at its extrema that has curved over length-scale L to move away from a pinning site by a distance b. Red dots along the z-axis indicate pinning sites at the unpinned edges of the vortex, and the dashed line shows the range of the pinning potential.

what is achievable in an NS. From equation (A13), we see that, for a given pinning energy (i.e. fixed V_{cr}), the critical unpinning velocity has a minimum of $\bar{V}_{cT} = V_{cr}$ once L is large enough. We can estimate that bending to unpin is possible when tension no longer increases the critical unpinning velocity. This will be the case if unpinning occurs over length-scales

$$L \gtrsim \sqrt{\frac{\nu R_{range}}{V_{cr}}} \tag{A14}$$

and if we approximate the critical velocity as $V_{cr} \approx E_p/(\rho_n \kappa R_{range} L)$, we find

$$L \gtrsim \frac{T R_{range}^2}{E_p}. \tag{A15}$$

We can reasonably assume that $R_{range} \approx r_c$, and since $r_c \approx R_{ws}$ (within a factor of less than 2 for $\beta = 3$, see Table 2), we finally obtain $L/R_{ws} \approx (TR_{ws})/E_p \approx 10^3$ for the unpinning length-scale in the deep crust, as estimated from energetics in Section 2.3.

This paper has been typeset from a TEX/LATEX file prepared by the author.